Available online at www.sciencedirect.com
ScienceDirect
Journal of Power Sources 173 (2007) 264–276
JOURNAL OF POWER SOURCES
www.elsevier.com/locate/jpowsour

Numerical studies on an air-breathing proton exchange membrane (PEM) fuel cell stack

Y. Zhang, A. Mawardi, R. Pitchumani *

Advanced Materials and Technologies Laboratory, Department of Mechanical Engineering, University of Connecticut, Storrs, CT 06269-3139, United States

Received 27 February 2007; received in revised form 1 May 2007; accepted 3 May 2007
Available online 22 May 2007

Abstract

Air-breathing proton exchange membrane (PEM) fuel cells provide for fully or partially passive operation and have gained much interest in the past decade, as part of the efforts to reduce the system complexity. This paper presents a detailed physics-based numerical analysis of the transport and electrochemical phenomena involved in the operation of a stack consisting of an array of vertically oriented air-breathing fuel cells. A comprehensive two-dimensional, nonisothermal, multi-component numerical model with pressurized hydrogen supply at the anode and natural convection air supply at the cathode is developed and validated with experimental data. Systematic parametric studies are performed to investigate the effects of cell dimensions, inter-cell spacing and the gap between the array and the substrate on the performance of the stack. Temperature and species distributions and flow patterns are presented to elucidate the coupled multiphysics phenomena. The analysis is used to determine optimum stack designs based on constraints on desired performance and overall stack size.
© 2007 Elsevier B.V. All rights reserved.

Keywords: Proton exchange membrane (PEM) fuel cell; Air breathing; Numerical model; Temperature distribution; Species distribution; stack

1. Introduction

Increasing energy requirements around the world have stimulated the interest to develop new reliable clean energy to decrease the dependence on fossil fuels and to reduce atmospheric pollution. To this end, proton exchange membrane (PEM) fuel cells are a strong alternative as a portable power source in widespread applications including automotive, laptop computers, cellular phones and other electronic devices owing to its low operating temperature, quick start, light weight and high power density. Recently, air-breathing PEM fuel cells have gained much interest due to their compact size and fewer components. Since oxygen is drawn directly from the atmosphere by natural convection, humidification and pressurization subsystems at the cathode are no longer required, which forms the basis of the reduced system complexity.

Effective design of air-breathing PEM fuel cells requires a thorough understanding of the interrelated heat and mass transport phenomena and electrochemical reactions in the cell, which has motivated the studies in the literature. Earlier experimental and numerical investigations on air-breathing PEM fuel cells focused on the performance evaluation and design of a single fuel cell. Several materials and fuel cell designs were explored [1–3], while analytical model and numerical simulations from physics-based models were used to predict the performance of the cell and to obtain detailed species and temperature distributions inside the cell [4,5]. A new design of an air-breathing fuel cell was reported by the authors [6], who also presented detailed computational modeling of the cell performance. The design consists of a dual fuel cell cartridge with a common hydrogen flow channel and two exposed cathode surfaces in communication with the ambient air.

The studies on individual air-breathing fuel cells have shown the practical viability of the designs. Meeting the power requirements of practical applications requires configuring multiple individual air-breathing cells connected either in series or in parallel as needed to form a stack. To the best of the authors' knowledge, relatively scant work on air-breathing fuel cell stacks has been reported in the open literature. Chu et al. [7,8] reported

* Corresponding author. Tel.: +1 860 486 0683; fax: +1 860 486 5088.
E-mail address: pitchu@engr.uconn.edu (R. Pitchumani).

0378-7753/$ – see front matter © 2007 Elsevier B.V. All rights reserved.
doi:10.1016/j.jpowsour.2007.05.008

Nomenclature

a	water vapor activity
A	fuel cell active area (m^2)
c_f	fixed charged site concentration in membrane ($mol\,m^{-3}$)
c_p	specific heat at constant pressure ($J\,(kg\,K)^{-1}$)
D_i	diffusivity of species i ($m^2\,s^{-1}$)
E_{cell}	cell voltage (V)
E_{stack}	stack voltage (V)
F	Faraday's Constant ($Coulomb\,mol^{-1}$)
$\vec{g}$	gravity vector ($m^2\,s^{-1}$)
h	vertical gap (m)
H	stack height (m)
I	average current density ($A\,m^{-2}$)
j	transfer current density ($A\,m^{-3}$)
k	permeability of porous media or equivalent porous media (m^2)
k_ϕ	electrokinetic permeability of membrane (m^2)
k_p	hydraulic permeability of membrane (m^2)
k_t	thermal conductivity ($W\,(m\,K)^{-1}$)
L_s	stack length (m)
M_i	molecular weight of species i ($kg\,s^{-1}$)
m	flow rate (lpm)
p	pressure (Pa)
p_{sat}	saturation pressure of water vapor in Eq. (11)(bar)
RH	relative humidity
S	source terms of governing equations in Table 1
T	temperature (K)
$\vec{V}$	superficial velocity vector ($m\,s^{-1}$)
$\mathbf{V}$	volume of the catalyst layer (m^3)
x	position coordinate across the cell thickness/the membrane
x_i	mole fraction of species i
y_i	mass fraction species i
y	position co-ordinate along the chamber
z_f	charge of sulfonate site in the membrane

Greek letters

α	transfer coefficient
ε	porosity
ε_{mc}	volume fraction of membrane in the catalyst layer
ϕ	phase potential (V)
η	surface over potential (V)
λ	water content
ρ	fluid density ($kg\,m^{-3}$)
σ	electrical/protonic conductivity ($1\,(ohm\,m)^{-1}$)
$\vec{\tau}$	stress tensor ($kg\,(m\,s)^{-2}$)

Subscripts/superscripts

a	anode
ave	average
c	cathode
eff	effective value
f	fluid
H_2	hydrogen
i	species
m	membrane
O_2	oxygen
ref	reference
s	solid
t	thermal
w	water
x, y	component values along the x and y coordinate directions

experimental tests combined with numerical analysis based on empirical correlations to evaluate the steady-state performance of an air-breathing PEM fuel cell stack under different operating conditions, while Morner and Klein [9] presented the dynamic behavior of an air-breathing fuel cell stack and the influence of temperature, humidity and air flow on the stack performance. Most recently, Litster and Djilali [10] implemented an empirical correlation for membrane conductivity to improve the accuracy of the modeling for dry membrane condition and the model was well validated with experimental data. A comprehensive parametric study was conducted to investigate the effects of design specifications and operating conditions on the cell performance. The fundamental difference between the conventional and the air-breathing fuel cell stacks is that in a conventional PEM fuel cell stack, the stack geometry and dimensions affect only the heat transfer characteristics, while in an air-breathing stack the internal and external stack designs affect both the heat transfer and the gas supply directly.

A comprehensive analysis of the governing multiphysics phenomena is imperative for effective stack designs and forms the focus of the present work. Considering the dual-fuel-cell cartridge design, described in Ref. [11], the study focuses on the analysis of a stack of such cartridges. The stack is configured as a vertical array of equally-spaced cartridges on a horizontal substrate, with a clearance between the substrate and the bottom face of the cartridge. The inter-cartridge spacing, the gap between the cartridge and the substrate, as well as the cartridge dimensions affect the natural convective flow patterns at the cathode faces that influence the stack performance. This paper presents numerical studies with the objective of systematically analyzing the effects of the stack height, the gap above the horizontal substrate, and spacing between cartridges on the performance of an air-breathing PEM fuel cell stack. A comprehensive two-dimensional physics-based model is developed based on the model for a single cell presented in Ref. [11], and extended to include the effects of adjacent cartridges as well as the substrate underneath the cartridges. The numerical model is first validated with experimental data, which forms the basis for identification of the optimum stack parameters for maximizing performance subject to constraints on overall stack size. The numerical model adopted in the present study is presented in the next section, and the results of the studies are discussed in Section 3.

Table 1
Source terms in the governing equations for the various regions of the fuel cell

Region	S_c	S_V	S_T	S_i	S_s, S_m
Gas channels	0	0	0	0	0
Diffusion layers and metal meshes	0	$-\frac{\mu}{k}\varepsilon_{\text{eff}}\vec{V}$	0	0	0
Catalyst layers	Anode: $-\frac{j_a}{2F}M_{H_2}$	$-\frac{\mu}{k_p}\varepsilon_{\text{eff}}\vec{V}+\frac{k_\phi}{k_p}z_f c_f F\nabla\phi_m$	Anode: $j_a\eta_a+\frac{i^2}{\sigma_m^{\text{eff}}}$	Anode: $-\frac{j_a}{2F}M_{H_2}$ (H_2), 0 (O_2), 0 (H_2O)	Anode: $S_s=-j_a<0$, $S_m=+j_a>0$
	Cathode: $-\frac{j_c}{4F}M_{O_2}+\frac{j_c}{2F}M_{H_2O}$		Cathode: $-j_c\eta_c+\frac{i^2}{\sigma_m^{\text{eff}}}$	Cathode: 0 (H_2), $-\frac{j_c}{4F}M_{O_2}$ (O_2), $\frac{j_c}{2F}M_{H_2O}$ (H_2O)	Cathode: $S_s=+j_c>0$, $S_m=-j_c<0$
Membrane	0	$-\frac{\mu}{k_p}\varepsilon_{\text{eff}}\vec{V}+\frac{k_\phi}{k_p}z_f c_f F\nabla\phi_m$	$\frac{i^2}{\sigma_m^{\text{eff}}}$	0	0

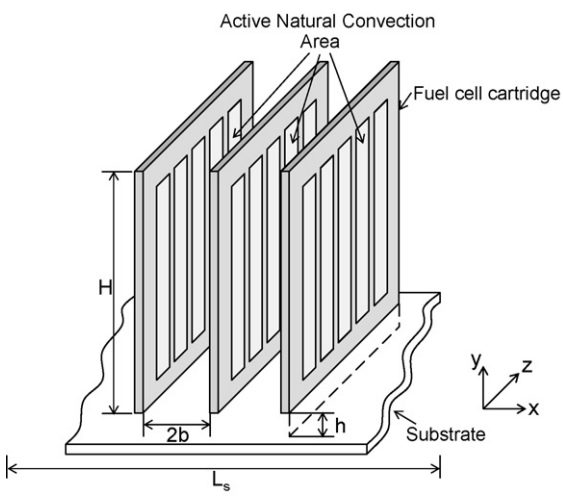

Fig. 1. Schematic of an air-breathing PEM fuel cell stack.

2. Mathematical model

Fig. 1 shows a schematic description of an air-breathing PEM fuel cell stack, consisting of an equispaced array of air-breathing fuel cell cartridges oriented vertically on a substrate. The stack parameters considered in this study are shown in Fig. 1: stack length, L_s; stack height, H; spacing between two adjacent fuel cell cartridges, $2b$; and vertical gap between the stack and the bottom substrate, h.

Each air-breathing fuel cell cartridge in the stack consists of two single cells sharing a common hydrogen flow chamber on their anode sides, while the cathode sides of the two cells are exposed to ambient air. Fig. 2 shows an exploded schematic illustration of a two-dimensional cross section of the assembled cartridge spanning across the thickness of the cell (x-direction) and along the length of the hydrogen chamber (y-direction). Each cell in the cartridge comprises a layered structure of seven components as identified in one of the cells in Fig. 2: (1) an outermost frame with ribs to provide overall support; (2) a cathode metal mesh which acts as cathode current collector; (3) a cathode gas diffusion layer (GDL); (4) a membrane electrode assembly (MEA), consisting of a proton transport membrane and two catalyst layers on its surfaces where electrochemical reactions take place; (5) an anode gas diffusion layer; (6) an anode metal mesh which acts as anode current collector; (7) a common anode hydrogen flow chamber shared by the two cells. The component layers of the two cells are bolted together to form a cartridge. The two individual cells can be connected in parallel or series to meet the design requirements. The frames and the metal meshes serve to increase the stiffness of the cartridge and minimize the deformation of the fuel cell, and correspondingly decrease the interfacial contact resistances inside the cell. Due to the symmetry along the mid-line of the hydrogen channel and that of cartridge spacing, the computational modeling is based on the half domain of the cartridge, identified by the thick dashed line in Fig. 2. The bottom line of the domain is determined by the

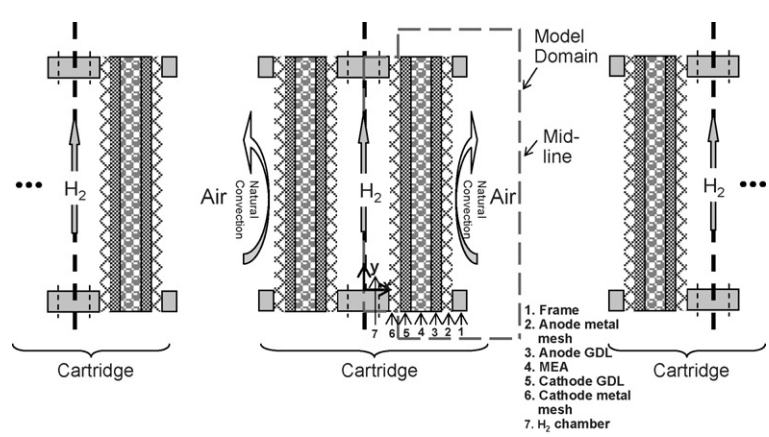

Fig. 2. Schematic illustration of a two-dimensional section of an air-breathing PEM fuel cell cartridge in the stack.

edge of the substrate and the top line is set to ensure the enough extension region to simulate the natural convection flow outside the cathode.

During the stack operation, hydrogen gas (H_2) is supplied into the anode chamber of individual cartridge at a constant flow rate through a manifold, while the cathode surfaces are exposed to the atmosphere and the required oxygen (O_2) is drawn into the cell from the ambient air around the stack by natural convection and diffusion. Therefore, the air flow pattern around the cathode side significantly affects the air supply at the cathode, which is determined by the geometry parameters of the stack including the cartridge spacing, $2b$, the vertical gap, h, and the stack height, H. More fresh air will be provided to the open cathode with increase of the cartridge spacing and the vertical gap, which improves the air transport into the cell and correspondingly enhances the cell performance at a cost of larger size of the stack. Increasing the stack height increases the flow path of air; however, the air concentration will decrease along the height due to the reaction consumption, which may cause insufficient oxygen availability toward the top of the stack.

To investigate the cell performance in the stack, a computational modeling is developed to describe the physical phenomena inside a single cell in a stack. The gas transport through the domain is governed by the coupled continuity, momentum, and species conservation equations; the water transport through the membrane from anode to cathode is modeled as source terms representing the osmotic drag, and is included in the momentum equations for the catalyst layers and the membrane; and the electron transport through the external circuit is governed by solid phase potential equation in the catalyst, gas diffusion layers and metal mesh at anode and cathode sides, while the proton transport in the MEA is expressed as membrane phase potential equation, in which the electrochemical reactions contribute as the source terms based on the Butler-Volmer expressions. The heat released from the electrochemical reactions and Joule heating heats up the stack and the surrounding ambient air and are included in the energy equation to solve for the temperature distribution inside the cell and between the cartridges, which drives the natural convection flow around the cell.

The assumptions for the present model follow those routinely adopted in the previous studies, namely: (1) the species are treated to be ideal gas mixtures; (2) the flow is assumed as laminar in the entire model domain; (3) liquid water is not considered due to the relatively low current density characteristic of air-breathing cells in comparison to conventional PEM fuel cells with forced cathodic flow; (4) the gas diffusion layers, catalyst layers and membrane are considered to be isotropic and homogeneous; (5) the membrane is considered impermeable to gas flow and crossover phenomena are not considered; (6) contact resistances are not considered; (7) Joule heating is only considered in the membrane and catalyst layers.

The coupled system of governing equations presented here is formulated to describe the entire half-domain in Fig. 2, with the phenomena specific to each region expressed in terms of appropriate source terms. This provides a unified formulation as summarized below with the specific source terms listed in Table 2:

$$\nabla \cdot (\rho \vec{V}) = S_c \tag{1}$$

$$\nabla \cdot (\rho \vec{V} \vec{V}) = -\nabla p + \nabla \cdot \vec{\tau} + \rho \vec{g} + S_V \tag{2}$$

$$\nabla \cdot (\rho \vec{V} y_i) = \nabla \cdot (\rho D_i^{\text{eff}} \nabla y_i) + S_i \tag{3}$$

$$\nabla \cdot (\rho c_p \vec{V} T) = \nabla \cdot (k_t^{\text{eff}} \nabla T) + S_T \tag{4}$$

$$\nabla \cdot (\sigma_j^{\text{eff}} \nabla \phi_j) + S_j = 0; \quad j = \text{s,m} \tag{5}$$

where ρ is the fluid mixture density; $\vec{V}$ the superficial (volume-averaged) velocity vector with components u in the x-direction and v in the y-direction to ensure mass flux continuity at the interface between porous and non-porous media of the domain; p the pressure; $\vec{\tau}$ the stress tensor; $\vec{g}$ the gravity vector, which is $0\,\text{m}\,\text{s}^{-2}$ in the horizontal direction and $9.8\,\text{m}\,\text{s}^{-2}$ in the vertical direction; y_i represents the i-th species mass fraction; c_p is the fluid specific heat at constant pressure; T is the temperature; and ϕ_s and ϕ_m denote the solid phase and membrane phase potentials, respectively.

The source terms in the governing equations represent physical phenomena specific to the various regions as follows: S_c is mass consumption or generation terms in the two catalyst layers; S_V represents the pressure gradient due to flow through porous media, and includes both pressure gradient due to flow through porous media and electroosmotic force in the MEA since protons are driven by osmotic force and transported from the anode catalyst layer to the cathode catalyst layer with water; S_i stands for the consumption of H_2 in the anode catalyst layer, and consumption of O_2 and the generation of H_2O in the cathode catalyst layer; S_T represents the heat generated in the catalyst layers due to reactions and Joule heating in the MEA. Joule heating in the solid phase is neglected since the electrical conductivity of the solid phase is much larger compared with the ionic conductivity in the MEA; the source term S_j denotes current generation owing to the electrochemical reactions in the two catalyst layers, expressed by transfer current densities. The expressions for these source terms are summarized in Table 1.

The species conservation equation (Eq. (3)) is applied to solve for the mass fractions of only $n-1$ species components, and the last component is calculated by:

$$y_n = 1 - \sum_{i=1}^{n-1} y_i \tag{6}$$

In the present study, since pure H_2 is supplied into the cartridges of the stack, the mass fraction of H_2, O_2 and H_2O – y_{H_2}, y_{O_2} and y_{H_2O} – are obtained from Eq. (3), and that of N_2, y_{N_2}, is calculated using Eq. (6).

The governing equation set involves several parameters that are determined using appropriate models as summarized below:

(1) The effective diffusivity of individual species in each region, D_i^{eff}, is modeled using Bruggeman correlation based on the

Table 2
Physical and geometry parameters used in the numerical simulations

Parameter	Symbol	Value	Source [Ref.]
Length of H_2 chamber, [cm]	H	1.68/5.00	Experiment [6]
Metal mesh (screen) width, [mm]		0.5	
Gas diffusion width, [mm]		0.3	
Catalyst layer width, [mm]		0.016	
Membrane width, [mm]		0.018	
H_2 chamber width, [mm]		3.2	
Permeability of diffusion layer [m^2]	k	2.97×10^{-9}	Experiment [6]
Gas diffusion porosity	ε	0.776	
Anode reference exchange current density [A/m^3]	$j_{a,ref}$	1.0×10^{8}	
Cathode reference exchange current density [A/m^3]	$j_{c,ref}$	3000	
Hydraulic permeability of membrane [m^2]	k_p	1.58×10^{-18}	[15]
Electrokinetic permeability [m^2]	k_ϕ	1.13×10^{-19}	
H_2O viscosity in the membrane [kg/(m·s)]	μ_{H_2O}	8.91×10^{-4}	
Anode/cathode transfer coefficient	α_a/α_c	0.5/2.0	
Fixed site charge	z_f	-1	
Membrane water porosity	ε_m	0.28	
Volume fraction membrane in catalyst layer	ε_{mc}	0.5	
Fixed charge concentration [$kmol/m^3$]	c_f	1.2	
H_2 diffusivity in catalyst layer and membrane [m^2/s]	D_{H_2cata}	2.59×10^{-10}	[17]
H_2 diffusivity in gas [m^2/s]	D_{H_2ref}	1.1×10^{-4}	
O_2 diffusivity in gas [m^2/s]	D_{O_2ref}	3.2×10^{-5}	
H_2O diffusivity in gas [m^2/s]	D_{H_2Oref}	7.35×10^{-5}	
O_2 diffusivity in catalyst layer and membrane [m^2/s]	D_{O_2cata}	8.328×10^{-10}	[14]

effects of porosity and tortuosity in the porous media [12]:

$$D_i^{\text{eff}} = \varepsilon_{\text{eff}}^{1.5} D_{i,\text{ref}} \left(\frac{T}{T_{\text{ref}}}\right)^{1.5} \left(\frac{p_{\text{ref}}}{p}\right) \tag{7}$$

in which, ε_{eff} is the porosity in the gas diffusion layers, catalyst layers and metal mesh and the equivalent porosity in the membrane, and $D_{i,\text{ref}}$ is the diffusivity of the species i at the reference temperature and pressure: $T_{\text{ref}} = 353\,\text{K}$ and $p_{\text{ref}} = 10,1325\,\text{Pa}$, listed in Table 2. Note that in the non-porous region, D_i^{eff} defaults to 0 in a solid ($\varepsilon_{\text{eff}} = 0$) or the temperature- and pressure-dependent individual species diffusivity in an open channel ($\varepsilon_{\text{eff}} = 1$).

(2) The effective thermal conductivity, k_t^{eff}, is expressed as follows in the porous regions [18]:

$$k_t^{\text{eff}} = \varepsilon_{\text{eff}} k_{t,\text{f}} + (1 - \varepsilon_{\text{eff}}) k_{t,\text{s}} \tag{8}$$

where $k_{t,\text{f}}$ and $k_{t,\text{s}}$ are thermal conductivities of fluid and solid, respectively.

(3) The effective electrical conductivity of solid phase, $\sigma_{\text{s}}^{\text{eff}}$, is expressed as a function of the effective porosity, ε_{eff}, and the electrical conductivity of the solid material, σ_{s}, as $\sigma_{\text{s}}^{\text{eff}} = (1 - \varepsilon_{\text{eff}})\sigma_{\text{s}}$; the effective membrane ionic conductivity in the catalyst layers can be expressed as:

$$\sigma_{\text{m}}^{\text{eff}} = \varepsilon_{\text{mc}}^{1.5} \sigma_m = \varepsilon_{\text{mc}}^{1.5} (0.5139\lambda - 0.326) \times \exp\left[1268\left(\frac{1}{303} - \frac{1}{T}\right)\right] \tag{9}$$

where ε_{mc} is membrane volume fraction in the catalyst layer, and the ionic conductivity in the membrane phase, σ_{m}, is expressed as the function of temperature, T, and the hydration parameter, λ, defined as water molecules per sulfonate group, in the membrane [13]. The hydration parameter, λ, is estimated by the following empirical expression [13], such that a value of λ larger than 14 indicates the presence of over-saturated water vapor in the membrane:

$$\lambda = \begin{cases} 0.043 + 17.81a - 39.85a^2 + 36.0a^3, & 0 \le a \le 1 \\ 14 + 1.4(a - 1), & 1 \le a \le 3 \end{cases} \tag{10}$$

where a is water vapor activity, expressed as $a = x_{\text{w}} p / p_{\text{sat}}$, in which, x_{w} is water mole fraction, and p_{sat} is the

temperature-dependent saturation pressure of water [13]:

$$\log p_{\text{sat}} = -2.1794 + 0.02953(T - 273.15) - 9.1837 \times 10^{-5}(T - 273.15)^2 + 1.4454 \times 10^{-7}(T - 273.15)^3 \quad (11)$$

In the above expression, the saturation pressure, p_{sat}, is in bar, and the temperature, T, is in Kelvin.

As indicated in Table 1, the source term S_j, j = s,m, in the potential equations can be determined by transfer current densities, j_{a} and j_{c}, governed by the Butler–Volmer equations:

$$j_{\text{a}} = j_{\text{a}}^{\text{ref}} \left(\frac{x_{\text{H}_2}}{x_{\text{H}_2,\text{ref}}} \right)^{0.5} \left[\exp\left(\frac{\alpha_{\text{a}} F}{RT} \eta_{\text{a}} \right) - \exp\left(-\frac{\alpha_{\text{a}} F}{RT} \eta_{\text{a}} \right) \right] \quad (12)$$

$$j_{\text{c}} = j_{\text{c}}^{\text{ref}} \left(\frac{x_{\text{O}_2}}{x_{\text{O}_2,\text{ref}}} \right) \left[\exp\left(\frac{\alpha_{\text{c}} F}{RT} \eta_{\text{c}} \right) - \exp\left(-\frac{\alpha_{\text{c}} F}{RT} \eta_{\text{c}} \right) \right] \quad (13)$$

in which, the subscripts a and c denote anode and cathode, respectively, j_{ref} is the reference volumetric transfer current density, α the transfer coefficient, x_{H_2} and x_{O_2} are the mole fractions of H_2 and O_2 in the catalyst layers, respectively, F is the Faraday constant, and η is the surface over potential defined as [16]:

$$\eta = \phi_{\text{s}} - \phi_{\text{m}} - E_{\text{ref}} \quad (14)$$

where E_{ref} is 0 at the anode and equals the temperature-dependent open cell voltage, $E_{\text{OC}} = 0.0025T + 0.2329$, on the cathode side, where the temperature, T, is in Kelvin [14].

The boundary conditions associated with the governing equations set are shown in Fig. 3. The mid-line of the hydrogen chamber and the mid spacing between cartridges are both assumed to be lines of symmetry due to geometry symmetry and nearly identical operation of each cartridge in the stack. In the present study, the substrate is considered to be a DC–DC power converter generating constant heat; therefore, a constant heat flux of 0.025 W m^{-2}was specified at the bottom surface of the domain. The interface conditions at any two adjacent layers in the domain are implicitly satisfied since the governing equations are formulated and implemented for the entire region as a single domain. Accordingly, the boundary conditions for the solid phase potential equation, namely, $\phi_{\text{s}} = 0$, at the interface of the hydrogen chamber and the metal mesh and $\phi_{\text{s}} = E_{\text{cell}}$ at the cathode surface are implemented at the outer left and right borders of the domain with infinite electrical conductivity in the hydrogen chamber region and in the extended ambient region. Since there is no proton transport outside the MEA, the boundary conditions for the membrane phase potential are zero proton flux at the interfaces of the catalyst layers and gas diffusion layers, which is implemented as zero ionic conductivity in the regions except the MEA. The boundary conditions at hydrogen inlet are specified velocity components, u, v; specified mass fractions corresponding to humidified hydrogen, $y_{\text{H}_2,\text{a}}$, $y_{\text{H}_2\text{O},\text{a}}$; specified anode temperature, T_{a}; while those at the hydrogen outlet are as follows: specified anode pressure, p_{a}, and zero gradients for other flow quantities.

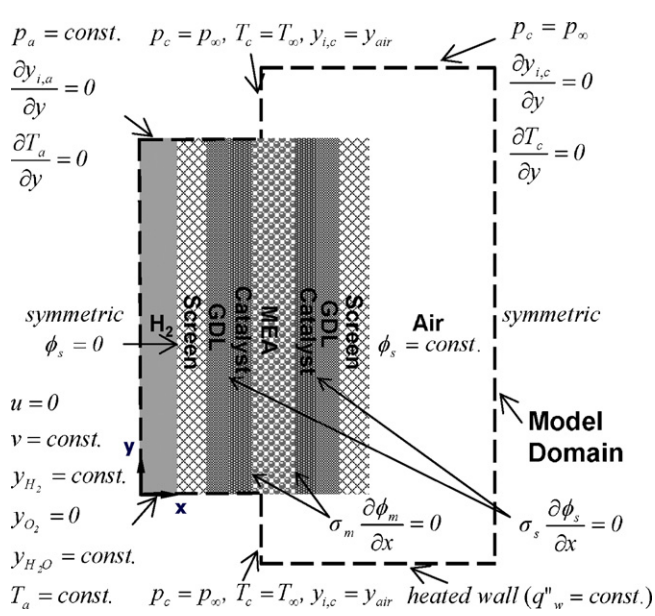

Fig. 3. Schematic of the model domain and the associated boundary conditions.

The model described above was implemented in a commercial finite-volume based computational fluid dynamics solver, *Fluent*, using the physical and geometry parameters listed in Table 2. Several user-written subroutines were embedded to describe mass consumption/generation, heat generation, water transport, electrochemical reactions and the potential equations as well as the effective properties for specific regions. A segregated implicit method was used to solve the coupled governing equations and the semi-implicit method for pressure-linked equations consistent (SIMPLEC) algorithm [19] was used for pressure correction to ensure mass conservation. No commercially available fuel cell module from *Fluent* was used. In the present study, the cells in the stack are considered to be connected in series and the performance of each cell is assumed identical in the stack. Therefore, the individual cell voltage, E_{cell}, which is one of the boundary conditions of the numerical modeling, is calculated as the stack voltage, E_{stack}, divided by the the number of the cells in the stack. Since each cartridge consists of two cells, the cell voltage, E_{cell}, is equivalently the stack voltage divided by twice the number of cartridges in the stack. According to the boundary conditions shown in Fig. 3, the coupled set of governing equations was solved iteratively to obtain the velocity, pressure, temperature, species and two potential distributions, from which the volumetric transfer current densities, j_{a} and j_{c} were calculated through Eqs. (12) and (13). The average current density of the fuel cell, I, is calculated by integrating the volumetric transfer current densities over the entire volume of the catalyst layer, and then dividing by the active area in the y–z plane (shown in Fig. 1), A, as:

$$I = \frac{1}{A} \int j_{\text{a}} \mathrm{d}\mathbf{V} = \frac{1}{A} \int j_{\text{c}} \mathrm{d}\mathbf{V} \quad (15)$$

Therefore, the polarization curve is constructed by solving for the average current density, I, for different values of cell volt-

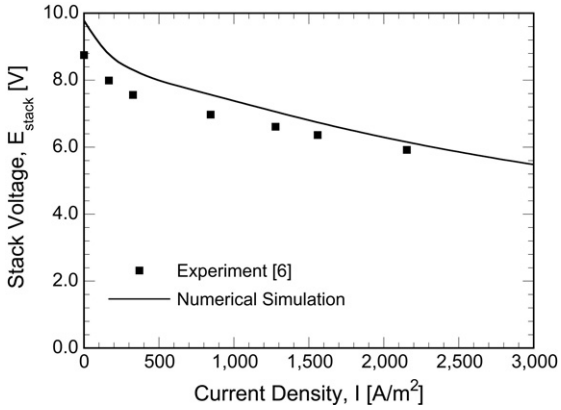

Fig. 4. Validation of the numerical simulations for the stack with experimental polarization curve data from Ref. [6].

age, E_{cell}. The convergence criterion is set as that the maximum scaled residual of all the variables being solved is less than 10^{-6}. The numerical simulations were used to explore the cell performance over a range of geometry parameters and the results are presented in the following section.

3. Results and discussion

The two-dimensional physics-based model presented in the previous section is first validated with experimental data from an air-breathing PEM fuel cell stack [6] consisting of cartridges as described in Fig. 2. Also, the numerical model was validated with the experimental data on the single cell performance for different operating conditions in Ref. [11]. Fig. 4 presents the comparison of polarization curves from the numerical simulation denoted as the solid line, and the experimental data from Ref. [6] described by the solid markers, for a stack consisting of five fuel cell cartridges, each of height, $H = 5.0$ cm, with cartridge spacing of $2b = 20.0$ mm, and vertical gap of $h = 15.0$ mm. The ten cells in the five cartridges are connected in series, and the current is collected through a square active area of 25 cm^2. The stack operating conditions are as follows: room temperature at the anode, $T_a = 298$ K, anode pressure, $p_a = 1.0$ atm, zero anode relative humidity, $RH_a = 0.0$, and constant anode flow rate for each cartridge, $m_a = 0.15$ lpm, while the cathode boundary conditions are as shown in Fig. 3. For the following discussion in this section, the above operating conditions are referred to as the base operating conditions. The stack voltage is calculated by multiplying the cell voltage from the numerical simulation by ten, the number of cells in the stack used in the experimental study [6]. It is seen in Fig. 4 that the stack voltage, E_{stack}, decreases monotonically with increase of the average current density, I, as expected due to ohmic loss in the membrane, and activation and concentration losses in the catalyst regions. The model predictions in Fig. 4 show a close agreement with experimental data, which forms a reliable basis for the use of the present numerical model to conduct systematic parametric studies. Since the stack voltage is directly related to each individual cell voltage by the number of cells, in the following discussion, the performance of a single cell in the stack is investigated.

Fig. 5 presents the temperature contours and corresponding flow patterns in the modeling domain for different vertical gaps and cartridge spacings, and for a fixed cell voltage of $E_{cell} = 0.5$ V and stack height of $H = 5.0$ cm under the base operating conditions. The temperature variation is represented by the dashed contour lines with corresponding temperature values in Kelvin and the stream lines are represented by the solid lines with arrows indicating the flow direction. The effects of vertical gap on temperature distributions and flow patterns are shown in Fig. 5a, where the cartridge spacing is fixed at $2b = 20.0$ mm. It is observed that the maximum cell temperature is approximately 303 K and the temperature variation inside the fuel cell is relatively small, around 1 K. The average temperature in the inter-cartridge space is seen to decrease with increasing vertical gap, which can further be explained from air flow patterns for different vertical gaps. If the bottom of the stack touches the top of the substrate, i.e., $h = 0.0$, air flow forms a recirculating pattern in the half domain of the inter-cartridge space (shown in the leftmost frame in Fig. 5a), and therefore, only a limited amount of fresh ambient air could enter the circulation inside the inter-cartridge space from the top of the stack.

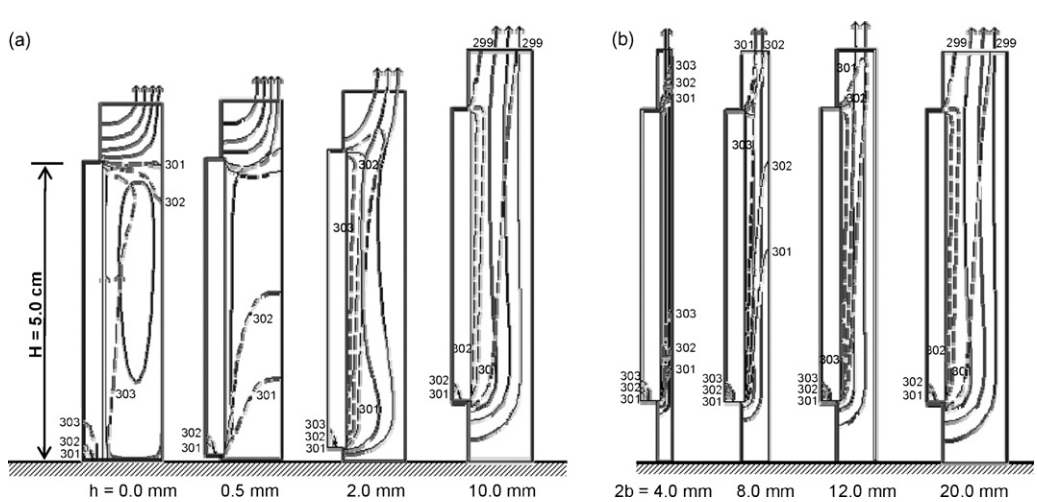

Fig. 5. Effects of (a) vertical gap, h, and (b) cartridge spacing, $2b$, on the temperature distributions and flow patterns of an individual cell in the stack at $H = 5.0$ cm.

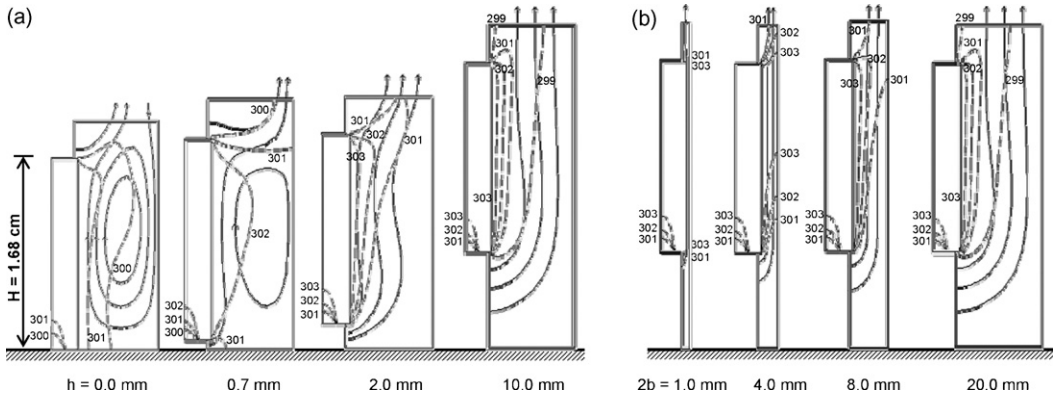

Fig. 6. Effects of (a) vertical gap, h, and (b) cartridge spacing, $2b$, on the temperature distributions and flow patterns of an individual cell in the stack at $H = 1.68$ cm.

As vertical gap increases, ambient air flows from the vertical gap and ascends along the entire height of the cartridge to provide natural convective cooling which leads to lower average temperature in the cartridge space. If the vertical gap is larger than a certain critical value, the temperature in the middle of cartridge space is reduced to room temperature (lower than 299 K in the plot), signifying that the convective flow pattern for an individual cell in the stack is no longer affected by the adjacent cells.

The effects of cartridge spacing on temperature distributions and flow patterns are shown in Fig. 5b, where the vertical gap is fixed at the largest value studied, $h = 10.0$ mm, and the spacing is varied from $2b = 4.0$ mm to $2b = 12.0$ mm. It is seen that the temperature distributions and flow patterns are similar for the different cartridge spacings. However, the temperature value is seen to be higher for small cartridge spacings due to the proximity effects of the adjacent cells. Fig. 6a and b show the temperature distributions and flow patterns under different vertical gaps and cartridge spacings for a shorter stack height of $H = 1.68$ cm. The temperature distributions and flow patterns have the same qualitative trends as those for the larger stack height of $H = 5.0$ cm in Fig. 5. The results indicate that variation in the stack height has the least effect on the thermal and fluid transport characteristics of the fuel cell stack, as opposed to the cartridge spacing, $2b$ and vertical gap, h, which significantly affect the temperature distribution and the flow patterns in the fuel cell stack.

The effects of vertical gap, h, and cartridge spacing, $2b$, on the cell performance for the stack height, $H = 5.0$ cm, are shown in Fig. 7. Fig. 7a presents polarization curves of an individual cell in

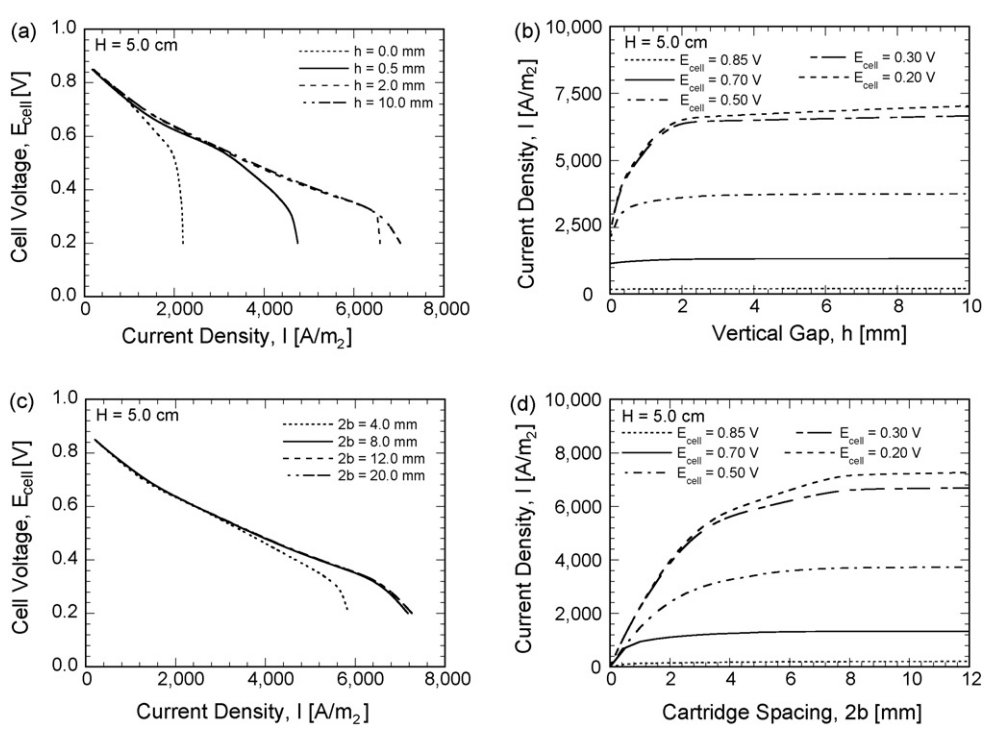

Fig. 7. The performance of an individual cell in the stack under different vertical gaps, h, and cartridge spacings, $2b$, at $H = 5.0$ cm: (a) the polarization curves for different h; (b) the current density variation with h for different cell voltages; (c) the polarization curves for different $2b$; (d) the current density variation with $2b$ for different cell voltages.

the stack with different vertical gaps, h, at a fixed cartridge spacing of $2b = 20.0$ mm. Note that with increase of h from 0.0 mm to 0.5 mm, the cell performance is significantly improved, while with increase of h from 0.5 mm to 2.0 mm, the cell performance only slightly improves, and with further increase of h from 2.0 mm to 10.0 mm, the performance remains the same, which indicates that beyond a certain clearance between the cartridge and the bottom substrate, the cell performance cannot be enhanced further with increase of h. This trend is corroborated by the flow patterns in Fig. 5a, which shows that increasing h to a non-zero value completely changes the flow patterns in the inter-cartridge space, whereby fresh ambient air is continuously drawn through the inter-cartridge space from the bottom to the top and results in enhanced oxygen transport into the cell for reactions. This pattern is improved with increasing of h from 0.5 mm to 2.0 mm in Fig. 5a; however, further increase of h results in no significant difference in the flow patterns. Correspondingly, the cell performance is seen to be only slightly improved for $h = 2.0$ mm to $h = 10.0$ mm since the cell reaches oxygen transportation limitation and no more improvement in the cell performance can be obtained from increasing the oxygen availability at the cathode. Fig. 7b shows the influence of h on the average current density for different values of E_{cell}: 0.2 V, 0.3 V, 0.50 V, 0.70 V and 0.85 V. It is seen that for the larger cell voltages of $E_{cell} = 0.85$ V and 0.70 V, the average current density is nearly invariant with the vertical gap, h, due to the small oxygen consumption at these cell voltages and the relatively sufficient oxygen supply even for a small clearance or no clearance. With decreasing cell voltage to $E_{cell} = 0.50$ V, 0.30 V and 0.20 V, the current densities increase sharply with increase of h, and saturate for h exceeding a minimum value, h_{min}. As shown in Fig. 5a, increasing h from 0.0 mm improves the air supply at the cathode: for $h \leq h_{min}$, the fuel cell performance is limited only by the air supply and improving the air supply results in enhanced current density; however, further increase in h does not affect the current density owing to the air supply exceeding the need corresponding to the cell voltage. Furthermore, it is noted in Fig. 7b that the minimum height, h_{min}, above which the current density saturates increases with decreasing cell voltage.

The polarization curve of a single cell in the stack for different cartridge spacing, $2b$, and at a fixed vertical gap, $h = 10.0$ mm, is presented in Fig. 7c. The polarization curves overlap at the higher voltages or equivalently, the smaller current densities, indicating the negligible influence of cartridge spacing since the air supplied through the smaller inter-cartridge space is still sufficient for stack operation at the smaller current densities. As the cell voltage decreases, the current density decreases with the inter-cartridge spacing, and the effect is seen to be especially pronounced for $2b = 4.0$ mm. A small inter-cartridge space reduces the air flow rate from the bottom to the top in the space, as shown in Fig. 5b, and results in insufficient availability of oxygen for the electrochemical reactions, correspondingly impairing the cell performance. Fig. 7d depicts the influence of inter-cartridge spacing on the current density for different cell voltages. It is observed that current density initially increases with increase of cartridge spacing at different cell voltages since oxygen supply is increased in proportion to the inter-cartridge spacing. However, as the cell reaches its oxygen transport limit corresponding to each cell voltage, no additional benefit is realized by increasing the cartridge spacing and the current density is seen to saturate beyond a certain critical spacing. The critical cartridge spacing is noted in Fig. 7d to increase from about 1.2 mm for $E_{cell} = 0.85$ V to 8.0 mm for $E_{cell} = 0.20$ V.

Fig. 8 presents the effects of the vertical gap and the inter-cartridge spacing on the cell performance in the stack of a shorter height of $H = 1.68$ cm. The polarization curves for different vertical gap, h, and the fixed inter-cartridge spacing, $2b = 20.0$ mm, are presented in Fig. 8a, where it is shown that increasing the vertical gap from 0.0 mm to 2.0 mm improves the cell performance at low cell voltages since the flow patterns are improved and more air is supplied from the clearance as shown in Fig. 6a. Further increase in the vertical gap does not affect the performance due to the sufficient air supply relative to the transport limitation inside the cell. The same trend is also reflected in Fig. 8b, where for $E_{cell} = 0.35$ V and 0.20 V, the current densities are improved significantly by increasing h in the range of 0.0–2.0 mm. Comparing Figs. 7b and 8b, it is seen that for low cell voltages in the range of 0.5–0.2 V, the increase in the current density with h for $H = 5.0$ cm is larger than that for $H = 1.68$ cm, which indicates that the performance of the large cell is more sensitive to the change of the clearance, h. The effects of inter-cartridge spacing, $2b$, on the cell performance in the stack are presented in Fig. 8c and d, where it is observed that as in Fig. 7c and d, there is a critical inter-cartridge spacing beyond which the current density is relatively invariant with the spacing. Fig. 8d further shows that the critical cartridge spacing increases with decreasing cell voltage, which corresponds to increasing oxygen consumption. Furthermore, a comparison of Figs. 7d and 8d reveals that the critical value of inter-cartridge spacing is larger for the larger cell size for a given cell voltage. Figs. 7 and 8 show that a minimum (critical) vertical gap and inter-cartridge spacing are needed for maximizing stack performance, and that these values are a function of the stack height, H.

To further illustrate the effects of the vertical gap and cartridge spacing on the transport and electrochemical phenomena inside the fuel cell, it is worth examining the species distributions on the cathode side. Fig. 9a and b present oxygen and water distributions, respectively, on the surface of the cathode GDL as a function of the vertical location along the stack height, y, for different vertical gaps, h, and $H = 5.0$ cm. In Fig. 9a, it is observed that with no vertical gap between the fuel cell cartridges and the bottom substrate, i.e., $h = 0.0$ mm, the oxygen mass fraction in the mixture is very low at about 0.04 along most of the surface of the cathode GDL, and increases rapidly from 0.04 to 0.20 at the upper end of the stack, reaching toward the oxygen mass fraction in the atmosphere of 0.23. This trend is consistent with air flow patterns in the inter-cartridge space shown in Fig. 5a and the corresponding performance in Fig. 7a. Without a vertical clearance, the only source for oxygen is from the top of the stack, resulting in very low oxygen mass fraction available for the electrochemical reactions. As the vertical clearance increases, a continuous flow path from the bottom to the top of the stack is established, which provides increasing oxygen supply to the cathode GDL surface. This trend is evident in

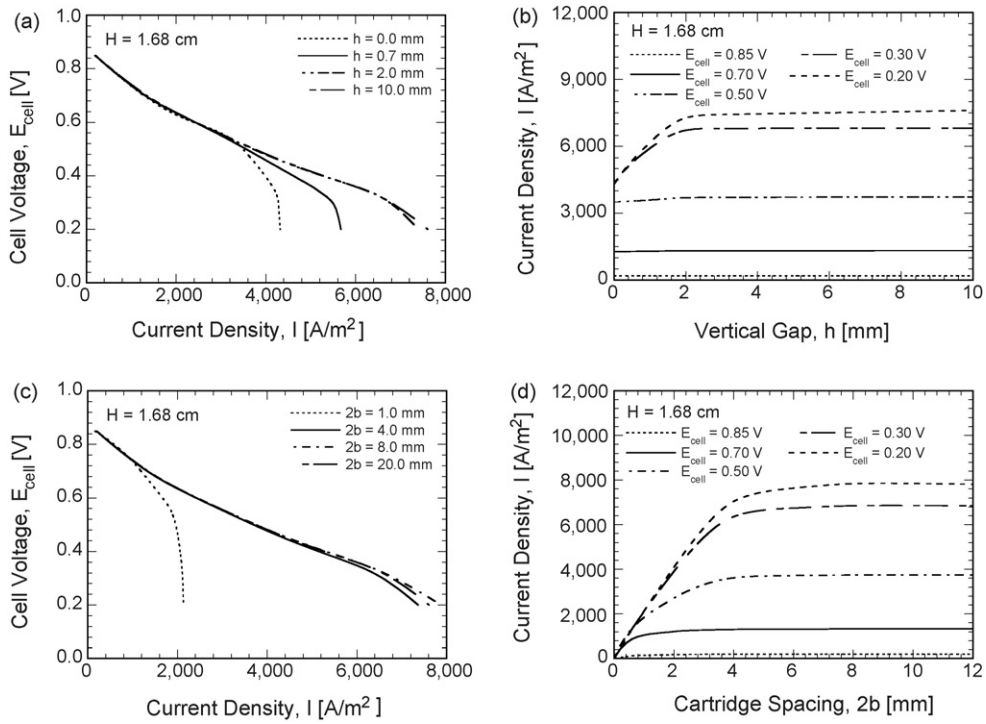

Fig. 8. The performance of an individual cell in the stack under different vertical gaps, h, and cartridge spacings, $2b$, at $H = 1.68$ cm: (a) the polarization curves for different h; (b) the current density variation with h for different cell voltages; (c) the polarization curves for different $2b$; (d) the current density variation with $2b$ for different cell voltages.

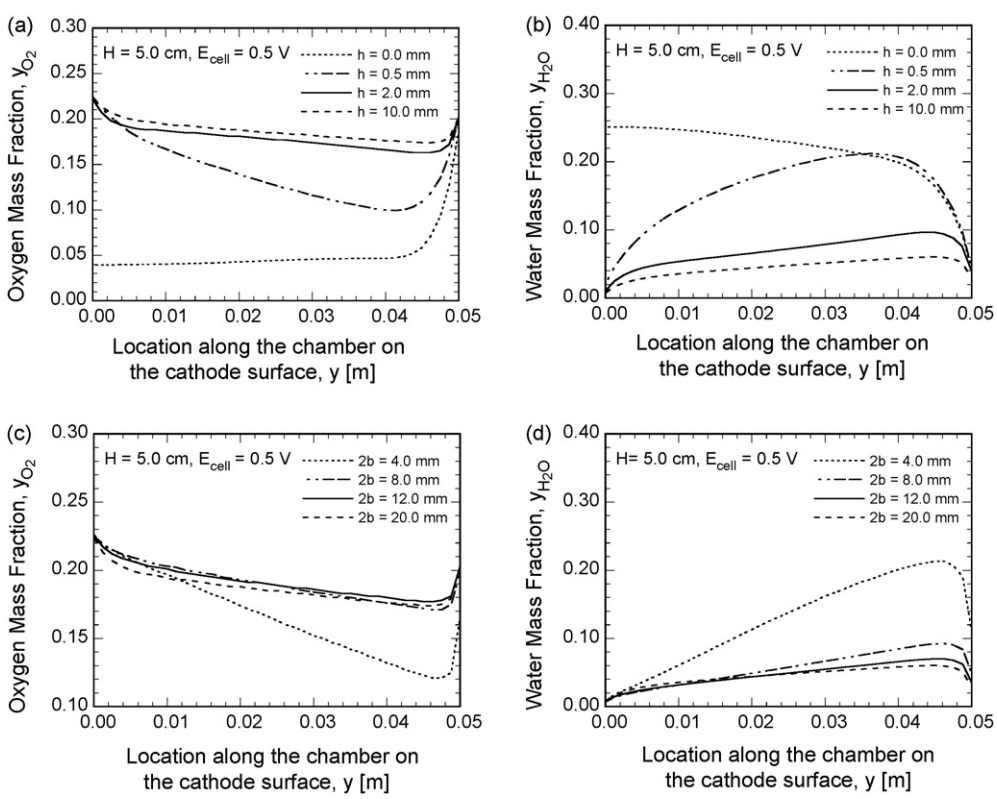

Fig. 9. Effects of vertical gaps, h, and cartridge spacings, $2b$ on species distributions along the cathode surface for $H = 5.0$ cm: (a) oxygen mass fraction distribution and (b) water mass fraction distribution for different h; (c) oxygen mass fraction distribution and (d) water mass fraction distribution for different $2b$.

the increasing oxygen mass fraction along the stack height in Fig. 9a for increasing values of h. For cases with $h > 0.0$ mm, as the location along the channel, y, increases from the bottom to the top, oxygen mass fraction initially decreases due to the rapid electrochemical reactions, and as y approaches the top of the stack, the oxygen mass fraction increases to the value close to that in the atmosphere. As h increases, the magnitude of the total oxygen mass fraction variation along the channel is seen to decrease due to improved oxygen supply. It is also observed that as vertical gap increases from 2.0 mm to 10.0 mm, oxygen mass fraction distribution increases only slightly, indicating a stabilization of the flow pattern and the oxygen supply relative to the need for the electrochemical reactions.

Water mass fraction distributions on the cathode GDL surface are shown in Fig. 9b corresponding to the conditions of the cell discussed in Fig. 9a. Using the water mass fraction distribution and the pressure and temperature distributions (Fig. 5), the relative humidity can be readily calculated. To compare with the oxygen mass fraction profiles shown in Fig. 9a, the water mass fraction instead of the relative humidity is presented and discussed here. In contrast to the oxygen mass fraction, the water mass fraction for a stack with no vertical clearance ($h = 0.0$ mm) is very high at the bottom of the cathode surface. As the flow patterns in Fig. 5a indicate, species including water are not effectively transported out of the cell, which leads to high water mass fraction on the surface at the bottom of the stack. Furthermore, the accumulated water practically blocks oxygen transport and results in degradation of the fuel cell and stack performance. As a vertical clearance is introduced by varying h from 0.0 mm to 2.0 mm, the water mass fraction on the cathode GDL surface decreases dramatically since the resulting flow pattern improves water transport, correspondingly reducing the concentration variation along the stack height. The water distribution also does not change appreciably as the vertical gap increases from 2.0 mm to 10.0 mm, following a pattern similar to that in the oxygen mass fraction profiles in Fig. 9a. The results in Fig. 9a and b indicate that a clearance of 2.0 mm or more may be optimum from a stack performance consideration.

Fig. 9c and d present the effects of cartridge spacing on the oxygen and water species distributions on the cathode GDL surface for the fixed vertical clearance of $h = 10.0$ mm. As cartridge spacing, $2b$, increases from the smallest value of 4.0 mm to 8.0 mm, the oxygen mass fraction values increase, while the magnitude of the total variation in the profiles along the cathode surface decreases owing to the improved oxygen supply. However, increasing cartridge spacing from 8.0 mm to 20.0 mm does not change the oxygen distribution as the fuel cell reaches the species transport limitations and does not benefit from the oversupply of air made available through the increased spacing. Water mass fraction distributions for different cartridge spacings are presented in Fig. 9d, where it is observed that the trend in the profiles is the opposite to that of the oxygen distributions. As cartridge spacing increases, water mass fraction along the surface decreases corresponding to the increase in the oxygen profile in Fig. 9c, and furthermore the variation in the value along the stack height also decreases. The profiles in Fig. 9c and d suggest that a spacing of 8.0 mm may be optimum from a stack design viewpoint.

Fig. 10 presents the oxygen and water distributions along the cathode GDL surface corresponding to the stack height of $H = 1.68$ cm. Oxygen mass fraction distributions on the surface for different vertical gaps are shown in Fig. 10a, where it is observed that the variations follow a similar trend to the results for the stack height of $H = 5.0$ cm in Fig. 9a, discussed previously. Fig. 10b shows the corresponding water mass fractions for different vertical gaps. A comparison of the results in Figs. 9a and 10a and those in Figs. 9b and 10b indicate that for the same vertical gaps, the values of the oxygen mass fraction are greater and the values of the water mass fractions are significantly lower for the smaller stack height, implying that for identical vertical gap and cartridge spacing, oxygen and water transport is improved by decreasing the stack height. Equivalently, the results imply that the value of the critical vertical clearance increases with increase in the stack height, H. Oxygen and water mass fraction distributions for different cartridge spacings are shown in Fig. 10c and d. As cartridge spacing decreases, the oxygen mass fraction decreases while water mass fraction increases, leading to a reduced performance of the stack. However, the magnitude of the decrease is smaller compared with that for the larger stack height, indicating that the minimum required cartridge spacing also deceases with a decrease in the stack height, H.

The performance analysis of an individual air-breathing cell in a stack, presented in the results so far, may be used towards the design of a stack, as illustrated in the discussion in the remainder of this section. The considerations underlying a stack design are generally (a) a prescribed voltage to be delivered by the stack, (b) maximization of the power density available of the stack, and (c) minimization of the overall stack dimensions. It was shown that increasing the clearance, h, and the inter-cartridge spacing, $2b$, improves the air flow patterns surrounding a cartridge and, in turn, the performance of the cartridge. However, increasing h and $2b$ also lead to increasing the dimensions of the stack. Similarly, a given voltage requirement from a stack may be realized by including many closely-spaced cartridges, each with a lower cell voltage due to the constricted flow patterns in the narrow inter-cartridge spaces, or a few appropriately spaced cartridges, each with a larger cell voltage enabled by the improved flow between the cartridges. In any case, a minimum number of cartridges is required to meet the voltage requirements. Thus, the stack design parameters to be determined from the analysis are: (1) the clearance of the cartridges from the substrate, h; (2) the (minimum) number of cartridges, N, required; (3) the inter-cartridge spacing, $2b$. For the discussion below, the cartridge height, H, is considered to be 5.0 cm, although the methodology outlined is equally applicable to any other value of H.

Based on the variation of the current density with the vertical clearance, h, for the different cell voltages in Fig. 7b, the clearance, h, is taken to be 2.0 mm from the observation that a larger clearance serves no useful effect on the performance improvement of the cell, whereas undesirably increases the overall stack height. The polarization curve corresponding to a clearance of 2.0 mm, such as that shown in Fig. 7c, is cast in terms of a cell

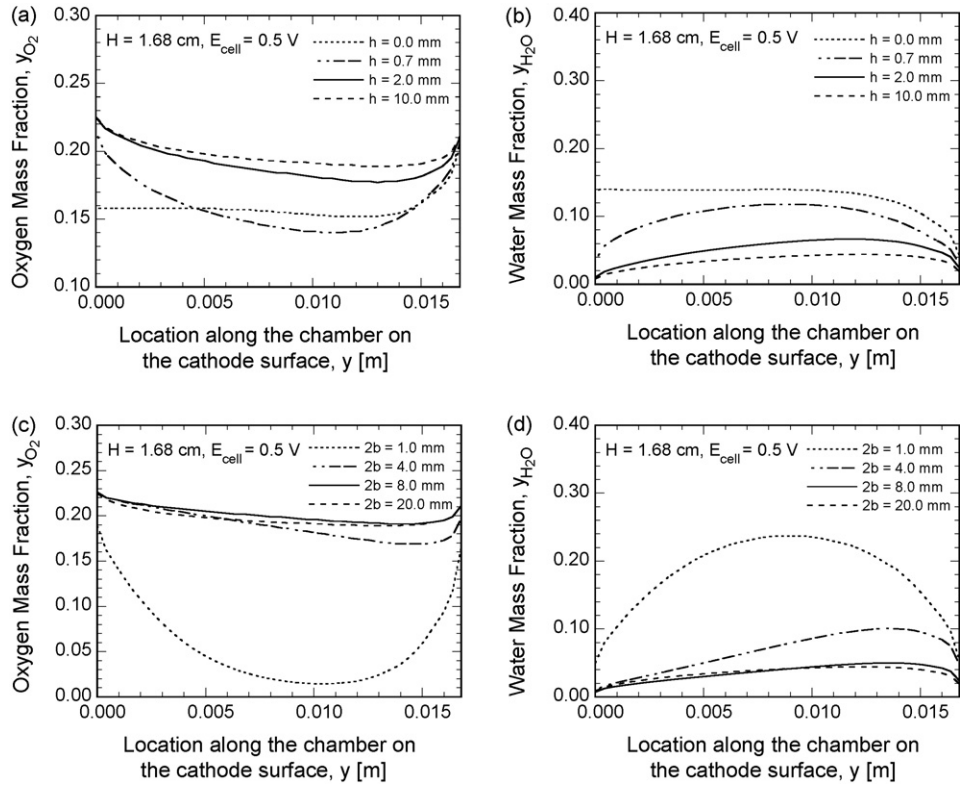

Fig. 10. Effects of vertical gaps, h, and cartridge spacings, $2b$ on species distributions along the cathode surface for $H = 1.68$ cm: (a) oxygen mass fraction distribution and (b) water mass fraction distribution for different h; (c) oxygen mass fraction distribution and (d) water mass fraction distribution for different $2b$.

voltage per unit stack length, E', by dividing the cell voltage by a nominal substrate length, $(b + 0.5t)$, associated with each cell (half cartridge), where t is the cartridge thickness (fixed at 6.5 mm in this study). Fig. 11a recasts the information contained in Fig. 7c in terms of a plot of the current density as function of the inter-cartridge spacing for four different values of the cell voltage per unit length, E'. The following observations are evident from Fig. 11a: all the lines converge to a current density of zero in the limit of the inter-cartridge space approaching zero, since physically the air supply at the cathode is cut off in the limit of zero spacing; for each value of E', there are two values of cartridge spacing, $2b$, that yield the same current density – one corresponding to operation at a higher cell voltage at a larger spacing (denoted as point A on one of the curves in Fig. 11a) and the other corresponding to operation at a lower cell voltage at a smaller cartridge spacing (denoted as point B in Fig. 11a) – although the total power density per unit stack length is identical for the two designs; and for each value of E', there is an optimum spacing that maximizes the current density output of the stack, and this optimum spacing as well as the associated maximum current density both increase with E'.

Fig. 11b presents the power density variation with the inter-cartridge spacing, for the four different values of E'. The plots are obtained from Fig. 11a by multiplying the cell voltage at every point in the lines. The results indicate an optimum spacing that maximizes the power density for each E', and a comparison with Fig. 11a reveals that the optimum spacing for maximum power density is larger than that maximizing the current density. This suggests that for a fixed voltage output from the stack, the design for maximum power density could be achieved with fewer cell cartridges (each operating at lower current density) than the number needed for maximizing the current density (which corresponds to a lower power density from the stack). Therefore, the design for maximum current density offers the largest power for a given stack length, while the design for the maximum power density provides for a lighter stack with fewer cartridges. The points of equi-current-density indicted as points A and B in Fig. 11a are also indicated in Fig. 11b to illustrate that the design with a larger inter-cartridge spacing (point A) has a higher power density compared to B with closely spaced cartridges, even though both designs offer the same current density and the same stack voltage for a given stack length.

Figs. 11a and b can be used as design charts for stack design as illustrated in the following example application which calls for a stack power, P_{stack}, and voltage, E_{stack}, of 40 W and 8 V, respectively, and a maximum stack length, L_s, of 80 mm. The specifications correspond to $E' = E_{\text{stack}}/L_s = 8/80 = 0.1\ \text{V mm}^{-1}$ with a series connection of the cartridges in the stack. From the viewpoint of minimizing the stack weight, the design point is set as that for the maximum power density, denoted as point C in Fig. 11b. Based on Fig. 11b, for $E' = 0.100\ \text{V mm}^{-1}$, the maximum power density is $1700\ \text{W m}^{-2}$ at an inter-cartridge spacing of $2b = 3.5$ mm. Therefore, the number of cartridges needed in the stack is: $N = L_s/(2b + t) = 80/(3.5 + 6.5) = 8$, which leads to the voltage for each cell, $E_{\text{cell}} = E_{\text{stack}}/2N = 8/(2 \times 8) = 0.5$ V. Also, for the same E'

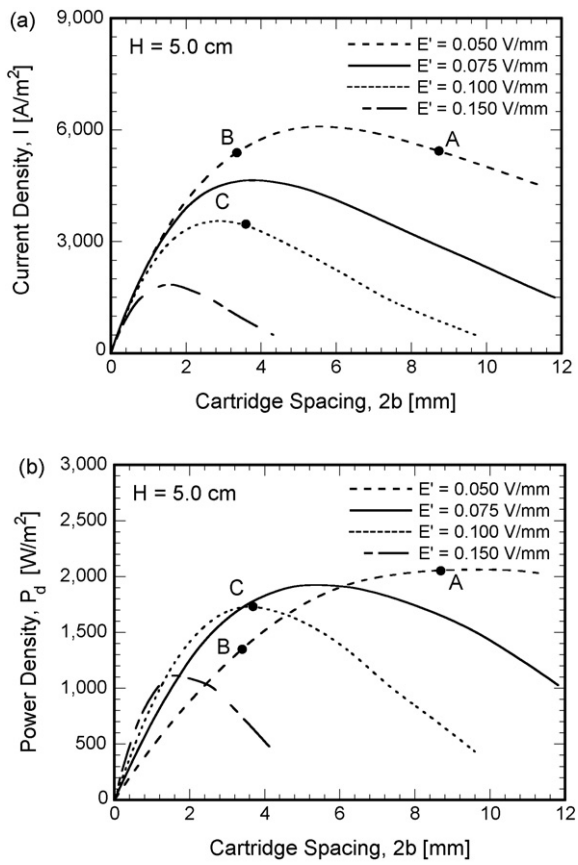

Fig. 11. Effects of cartridge spacing, $2b$, on (a) current density and (b) power density distributions at $H = 5.0$ cm.

and $2b$, the current density for point C in Fig. 11a is determined as $I = 3450\,\mathrm{A\,m^{-2}}$. Since the stack current is: $i_{\mathrm{stack}} = P_{\mathrm{stack}}/E_{\mathrm{stack}} = 40/8 = 5\,\mathrm{A}$, the active area of the fuel cell unit is: $A = i_{\mathrm{stack}}/I = 5/(3450 \times 10^{-4}) = 14.5\,\mathrm{cm}^2$. Since the cartridge height, H, is 5.0 cm in Fig. 11, the corresponding width of the cartridge is: $W = A/H = 14.5/5 \approx 3.0$ cm. The vertical clearance, h, is taken to be 2.0 mm since the stack performance is invariant above this value. The stack design is thus summarized as follows: $L_{\mathrm{s}} = 8.0$ cm, $H = 5.0$ cm, $W = 3.0$ cm, $h = 2.0$ mm, $2b = 3.5$ mm and $N = 8$, and the operating conditions are $E_{\mathrm{cell}} = 0.5$ V and $I = 3450\,\mathrm{A\,m^{-2}}$. This design methodology is applicable to any other specifications of application requirements and illustrates a physics-based approach to fuel cell stack design.

4. Conclusions

A comprehensive numerical analysis of a stack consisting of an array of air-breathing fuel cell cartridges was presented to illustrate the effects of the various stack and cell parameters, as well as the use of the analysis for stack design. It was shown that a critical minimum clearance between the fuel cell cartridges and the bottom substrate and a minimum inter-cartridge spacing were needed to enable the air flow patterns required for best performance of the stack. Furthermore, optimum spacings for two different objectives of maximizing current density and maximizing power density were developed and a comparative discussion of stack designs corresponding to these spacings was presented. The use of the analysis for design of a stack for target performance requirements and constraints was also illustrated. Overall, the study demonstrated the viability of air-breathing fuel cell for practical applications.

Acknowledgement

The authors gratefully acknowledge the support from the U.S. Army RDECOM through Contract No. DAAB07-03-3-K-415.

References

[1] A. Schmitz, M. Tranitz, S. Eccarius, A. Weil, C. Hebling, J. Power Sources 154 (2006) 437–447.
[2] T. Hottinen, O. Himanen, P. Lund, J. Power Sources 138 (2004) 205–210.
[3] F. Jaouen, S. Haasl, W. van der Wijingaart, A. Lundblad, G. Lindbergh, G. Stemme, J. Power Sources 144 (2005) 113–121.
[4] A. Schmitz, C. Ziegler, J.O. Schumacher, M. Tranitz, E. Fontes, C. Hebling, Fuel Cells 4 (2004) 358–364.
[5] C. Ziegler, A. Schmitz, M. Tranitz, E. Fontes, J.O. Schumacher, J. Electrochem. Soc. 151 (2004) A2028–A2041.
[6] R. Pitchumani, et al., Development of portable proton exchange membrane (PEM) fuel cell hybrid system and related technologies, Technical Report AMTL-0806–01, Advanced Materials and Technologies Laboratory, University of Connecticut, Storrs, CT, August 2006.
[7] D. Chu, R. Jiang, J. Power Sources 83 (1999) 128–133.
[8] D. Chu, R. Jiang, C. Walker, J. Appl. Electrochem. 30 (2000) 365–370.
[9] S.O. Morner, S.A. Klein, J. Solar Energy Eng. 123 (2001) 225–231.
[10] S. Litster, N. Djilali, Electrochim. Acta 52 (2007) 3849–3862.
[11] Y. Zhang, R. Pitchumani, Numerical studies on an air-breathing proton exchange membrane (PEM) fuel cell, Int. J. Heat Mass Transf., doi:10.1016/j.ijheatmasstransfer.2007.03.044, in press.
[12] R.B. Bird, W.E. Stewart, E.N. Lightfoot, Transport Phenomena, John Wiley and Sons, New York, 2006, pp. 793–799.
[13] T.E. Springer, T.A. Zawodzinski, S. Gottesfeld, J. Electrochem. Soc. 138 (8) (1991) 2334–2342.
[14] A. Parthasarathy, S. Srinivasan, A.J. Appleby, J. Electrochem. Soc. 139 (1992) 2530–2537.
[15] V. Gurau, H. Liu, S. Kakac, AIChE J. 44 (11) (1998) 2410–2422.
[16] S. Um, C.Y. Wang, K.S. Chen, J. Electrochem. Soc. 147 (2000) 4485–4493.
[17] H. Ju, C.Y. Wang, J. Electrochem. Soc. 151 (11) (2004) A1954–A1960.
[18] A. Bejan, Convection Heat Transfer, second ed., John Wiley and Sons, New York, 1995, pp. 566–638.
[19] S.V. Patankar, Numerical Heat Transfer and Fluid Flow, Hemisphere, Washington DC, 1980, pp.113–134.